Chemical Science

ROYAL SOCIETY OF CHEMISTRY

EDGE ARTICLE

View Article Online
View Journal | View Issue

Cite this: *Chem. Sci.*, 2025, **16**, 1857

All publication charges for this article have been paid for by the Royal Society of Chemistry

Received 12th July 2024
Accepted 7th December 2024

DOI: 10.1039/d4sc04639k

rsc.li/chemical-science

Harvesting ionic power from a neutralization reaction through a heterogeneous graphene oxide membrane†

Pei Liu,*[ad] Teng Zhou,[c] Linsen Yang,[b] Xin Li,[b] Lei Jiang[b] and Liping Wen*[b]

Nanofluidics is a system of fluid transport limited to a nano-confined space, including the transport of ions and molecules. The use of intelligent nanofluidics has shown great potential in energy conversion. However, ion transport is hindered by homogeneous membranes with uniform charge distribution and concentration polarization, which often leads to an undesirable power conversion performance. Here, we demonstrate the feasibility of a neutralization reaction-enhanced energy conversion process based on heterogeneous graphene oxide (GO) nanofluidics with a bipolar structure. The asymmetric charge distribution inherent to the heterogeneous nanofluidics facilitates a complementary two-way ion diffusion process, which in turn promotes efficient charge separation and superposed ionic diffusion. An output power density of up to 29.58 W m^{-2} is achieved with 0.1 M HCl/NaOH as the acid–base pair (ABP), which is about 712% and 117% higher than using symmetric unipolar pGO and nGO membranes. Both experiments and theoretical simulations indicate that the tunable asymmetric heterostructure contributes to regulating diffusion-based ion transport and enhancing the ion flux. This work not only establishes a significant paradigm for the utilization of chemical reactions within nanofluidic systems but also opens up new avenues for ground-breaking discoveries in the fields of chemistry, nanotechnology, and materials science.

Introduction

Exploring efficient and renewable energy sources is important to reduce dependence on fossil fuels and alleviate global environmental pollution.[1,2] Several sources of clean energy have been identified, including solar, wind, geothermal and water power.[3,4] However, these energy resources are intermittent and regional, and thus cannot meet the uninterrupted and long-lasting electricity demand for human activities and industry. Osmotic energy originates from the salinity gradient between sea and river water, and has become a popular research topic because of its abundance and wide distribution.[5–7] To effectively capture this energy, reverse electrodialysis (RED) technology and nanofluidics for high-performance osmotic energy harvesting have been developed in the past decade.[8–10] Large amounts of acids and bases are widely used in various industrial processes such as electroplating, dyeing, papermaking. The waste acid and alkali solutions generated in the process are usually treated by direct neutralization and discharged into the environment, which not only causes serious environmental problems but is also a huge waste.[11,12] Energy generation from the waste acid and base solutions can be achieved by RED with the aid of acid–base neutralization, which is environmentally and economically advantageous.[13–15] In a typical half-cell nanofluidics-based osmotic energy harvesting process, a high-salinity solution is separated from a low-salinity solution by a cation-selective or anion-selective membrane. The directional migration of cations or anions creates an ionic flux to generate electrical power. When the high-salinity and low-salinity solution are replaced by acid and base solutions, a pH gradient could be created. The H^+ (or OH^-) on one side can migrate across the nanofluidics system and meet the OH^- (H^+), forming H_2O immediately. Therefore, under the action of a neutralization reaction, the H^+ would be consumed, resulting in sustainable H^+ migration, which has shown great potential for energy harvesting.[16,17]

The emergence of two-dimensional (2D) lamellar nanofluidics systems consisting of stacked nanosheets offers new opportunities for the development of highly efficient energy conversion. Owing to the nanoconfined interlayer spacing, inherent surface charges, and high chemical resistance, these

[a]Henan Institute of Advanced Technology, Zhengzhou University, Zhengzhou 450052, China. E-mail: peiliu@zzu.edu.cn

[b]Key Laboratory of Bio-inspired Materials and Interfacial Science, Technical Institute of Physics and Chemistry, Chinese Academy of Sciences, Beijing 100190, China. E-mail: wen@mail.ipc.ac.cn

[c]College of Mechanical and Electrical Engineering, Hainan University, Haikou 570228, China

[d]College of Materials Science and Engineering, Zhengzhou University, Zhengzhou 450052, China

† Electronic supplementary information (ESI) available. See DOI: https://doi.org/10.1039/d4sc04639k

2D nanofluidic channels exhibit excellent ionic transport performance and acidic and basic stability, which is of great practical significance for neutralization assisted proton gradient-driven energy conversion power harvesting.[15,18] However, these 2D homogeneous nanofluidics systems with a single charge and significant concentration polarization exhibit intrinsic ion transport hindrance, resulting in an undesirable output power density.[19–21] Fortunately, it has been proved that multifunctional heterostructures could effectively impair the concentration polarization and achieve efficient ion selectivity. Moreover, built-in asymmetry can be readily obtained by the simple hybridization of homogeneous membranes.[22–27] Multilayer 2D GO membranes have attracted much attention due to their scalability, tunable ionic selectivity, chemical resistance, and physical stability, and can be used as a high-performance energy conversion device to harvest ionic power from the acid–base neutralization reaction.

Herein, we report a heterogeneous graphene oxide membrane (pnGO) based nanofluidic system for high-performance ionic power generation *via* acid–base neutralization (Fig. 1). By adopting the traditional neutralization reaction, the generated current of the system with 0.1 M HCl/NaOH as the acid–base pair (ABP) can reach about 1185.6 A m^{-2} thanks to the retained salinity gradients established by the neutralization reaction "$H^+ + OH^- \rightarrow H_2O$", which is much higher than that of the system without reaction participation (0.1 M NaCl and NaOH: ~78.6 A m^{-2}). Moreover, the heterogeneous nanofluidics system exhibits an asymmetric charge distribution, which improves the gradient-driven ion diffusion, allowing high-performance osmotic energy conversion with a power density of up to 29.58 W m^{-2} with 0.1 M ABP. To determine the role of the heterogeneous structure, a model system was proposed for finite-element simulations, which is used to better understanding the detailed ion transport. Molecular dynamics (MD) were performed to simulate the ion adsorption interactions between specific ions and nanosheets. Both experimental and theoretical results indicate that the synergistic effect of the inherent asymmetric charge and neutralization reaction would contribute to improving the ionic transport properties and eventually improve the energy conversion performance. This high-performance energy generation system can trigger further experimental and theoretical efforts to build intelligent

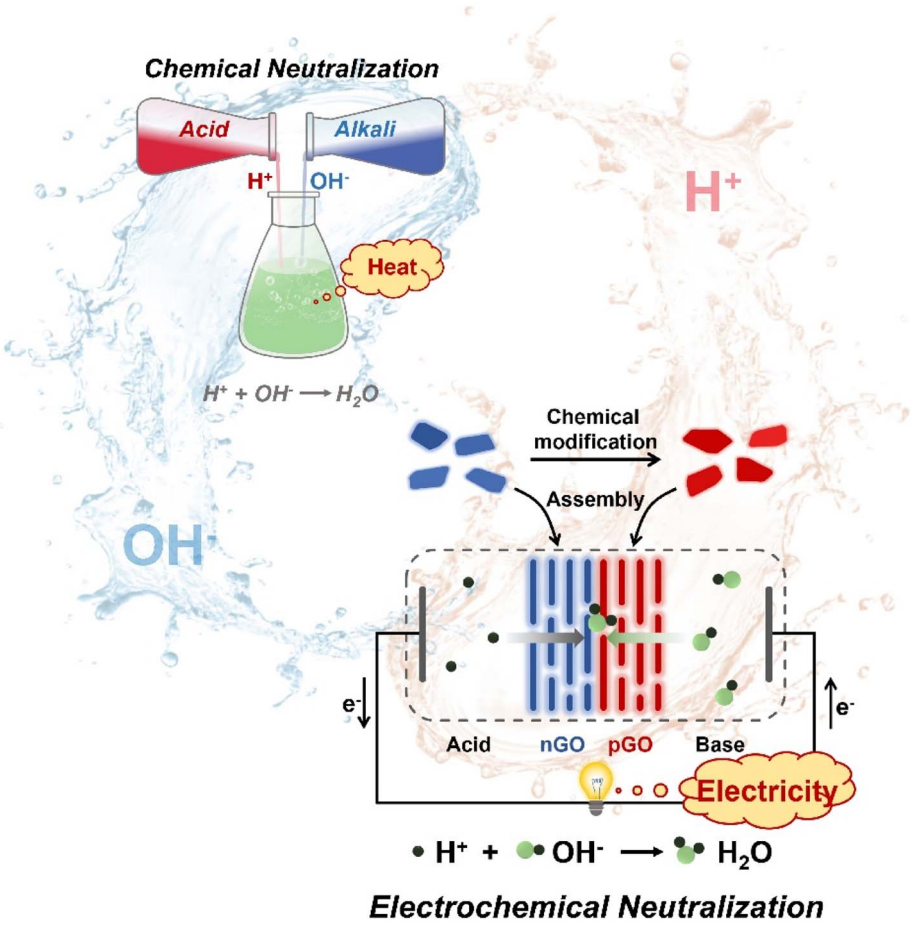

Fig. 1 Schematic representation of the heterogeneous GO-based electrochemical neutralization cell. Pristine GO nanosheets are negatively charged, and through chemical modification, positively charged GO nanosheets could be obtained. After stacking by vacuum filtration, oppositely charged heterogeneous graphene oxide membranes containing continuous 2D nanofluidic channels are generated to harvest ionic power from the acid and base solution.

heterogeneous nanofluidic systems for sustainable power generation from wastewater neutralization treatment processes, water purification, and desalination.

Results and discussion

Layered GO membrane fabrication and characterization

Pristine GO nanosheets are negatively charged (nGO) and typically several hundreds of nanometers to micrometers in lateral size (Fig. S1†). Positively charged GO nanosheets (pGO) were synthesized by the polyethyleneimine (PEI) modification method (Fig. S2, ESI†).[23,28] After chemical modification, the zeta potential of the GO colloids shifted from −31 mV to +33 mV at near neutral pH, indicating that the type of charge on the GO nanosheets had been changed. Both the nGO and the pGO colloids retain their charge properties over the pH range of 1 to 12 (Fig. 2a). Upon a two-step vacuum-assisted filtration process, free-standing and flexible heterogeneous graphene oxide membranes (pnGO) could be obtained (Fig. S3, ESI†). The cross-sectional image shows compactly packed lamellar structures of the membranes (Fig. 2b and S4†). Fourier transform infrared spectroscopy (FTIR) was employed to characterize the changes of functional groups after PEI modification (Fig. 2c). After PEI modification, a blueshift for the absorption band at 1730 cm^{-1} (–COOH) to 1624 cm^{-1} (–CO–NH–) is observed, confirming the conversion of the carboxyl groups to amide groups.[28,29] X-ray photoelectron spectroscopy (XPS) is used to further study the functional groups of the membranes (Fig. S5†), clearly showing the emergence of an N 1s peak. The single peak with strong intensity in the XRD pattern (Fig. 2d) suggests that the interlayer spacings of the nGO and pGO are 7.07 Å and 10.87 Å interlamellar spacings (ESI†) based on Bragg's law.[29–31] Given the theoretical thickness of a single layer GO nanosheet (3.34 Å),[5,29,32] the effective pathway for ion transport is calculated to be about 3.7 Å for dry nGO and 7.5 Å for dry pGO, and a sub-nano channel is constructed. In addition, the presence of typical peaks of both nGO and pGO in the XRD pattern of pnGO confirms its heterogeneous structure.

The membranes were then mounted in between a two-compartment electrochemical cell to investigate the ion transport properties (Fig. S6, ESI†). Fig. 2e shows the recorded current–voltage (*I–V*) curves in 0.01 M KCl. Due to their symmetric microstructure, the current density responses of both nGO and pGO membranes exhibit linear ohmic properties. Weak rectified ion-transport behavior is found through the heterogeneous pnGO membrane with an ionic current rectification (ICR) ratio of about 1.7 at 0.2 V. This result is in contrast to the symmetric *I–V* responses found in homogeneous nGO or

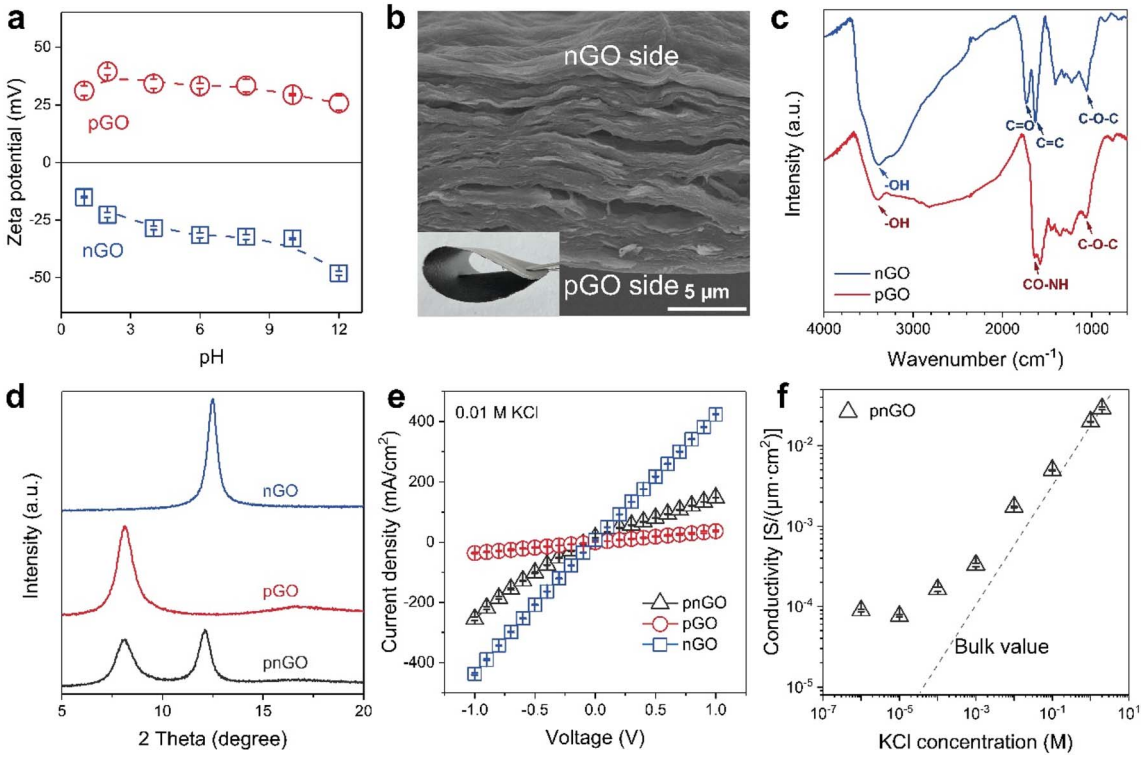

Fig. 2 Characterization of the layered GO membranes. (a) The zeta potentials of nGO colloids and pGO colloids (0.67 mg mL^{-1}) over the pH test range from 1 to 12. (b) Cross-sectional SEM image of the pnGO membrane showing compactly packed lamellar structures. (Inset) Photograph of the freestanding and flexible pnGO membrane. (c) FTIR spectra of nGO (blue) and pGO (red) membranes. (d) XPS of nGO and pGO. Sharp XRD peaks at 12.5° and 8.1° indicate a narrow inter-layer distance of about 0.70 nm for nGO and 1.08 nm for pGO. (e) Typical *I–V* curves of homogeneous pGO (red circle) and nGO (blue square) membranes show symmetric ion transport while the *I–V* curve of the pnGO membrane (black triangle) shows weak ICR. (f) Ionic conductivity of the pnGO membrane as a function of KCl concentration. The ionic conductivity gradually deviates from a linear relationship, indicating the surface charge governed ion transport.

pGO membranes.[33] As revealed by the zeta potentials results (Fig. 2a), the zeta potentials of the pGO and nGO nanosheets are completely opposite. Therefore, we can attribute the observed weak ICR effect to the asymmetric surface charge distribution. We further measured the ionic conductivity across the membranes as a function of KCl concentration (Fig. 2f and S7†). For all membranes, the transmembrane ionic conductivity shows distinct behavior down to 1 mM KCl. When the KCl concentration is over 1 mM, the conductivity increases linearly with the KCl concentration, similar to the bulk solution. The transmembrane ionic conductivity deviates from bulk behavior (gray dashed line) when the electrolyte concentration is less than 1 mM and gradually approaches a plateau, which indicates that the ion transport through the membranes is governed by the surface charge.[34–36]

Harvesting ionic power from the neutralization reaction

With a concentration difference, selective ion transport through a nanofluidics system converts a chemical gradient into a net diffusion current.[37,38] Similar to mixing two salt solutions with different concentrations, acid–base mixing can generate energy from acid–base neutralization. Considering the electrodes (Ag/AgCl) and the maximum concentration of NaOH (1 M) used here, 0.01 M NaCl was selected as the supporting electrolyte and all kinds of solution used in the acid–base systems contain 0.01 M NaCl (ESI†).[15,18] Here, HCl and NaOH as the acid–base pair (ABP) with the same concentration were set to the two compartments of the electrochemical cell, respectively, and the heterogeneous membrane is placed between them to explore the power generation performance. The nGO side faces the acid solution and the pGO side faces the base solution. As shown in Fig. 3a, the generated current density with 0.1 M ABP was about 1185.6 A m^{-2}, which is much higher than when using 0.1 M NaCl and NaOH (~78.6 A m^{-2}). The generated ionic power can be output by supplying an external load resistance. All the output current densities gradually decrease with increasing R_L (Fig. 3c), while the maximum output power ($P = I^2 \times R_L$) appears when R_L is equal to the internal resistance of the nanofluidic system (Fig. 3b).[9,39] The results showed that the maximum power density when using 0.1 M ABP (29.58 W m^{-2}) is much higher than when using 0.1 M NaCl/NaOH (1.37 W m^{-2}), which can be attributed to the acid–base neutralization reaction. Moreover, compared with the cell pair of "cation-exchange membrane (nGO) + neutral compartment + anion-exchange membrane (pGO)" with high resistance in the RED stack (Fig. S8†), the energy conversion performance can be improved significantly in the "combined" pnGO membrane system. The above results demonstrate that the pnGO has the potential for energy conversion from the neutralization reaction. In this process, as the nGO side holds the negative surface and pGO holds the positive surface, H^+ in the acid solution and OH^- in the base solution diffuse across the nGO and pGO, respectively, into the heterogeneous interface, and then react to produce water, which eventually diffuses out of the heterogeneous membrane. Thus, the H^+ and OH^- would be consumed, and the chemical potential gradient could be retained with the aid of the neutralization reaction, resulting in sustainable H^+ and OH^- migration, which could realize high-performance ionic power harvesting from the neutralization reaction.[14,15,17]

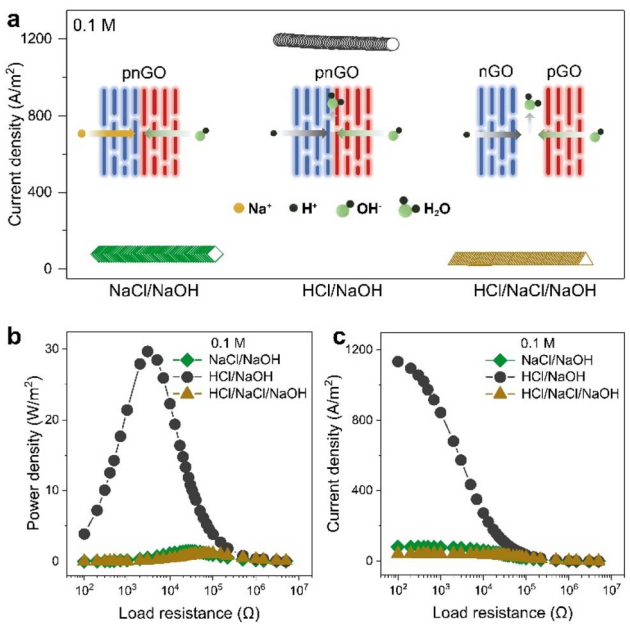

Fig. 3 Harvesting ionic power from neutralization reaction through heterogeneous pnGO membranes. (a) The recorded diffusion current density under three different test conditions. (Inset) Schematic illustration of the ion transport in heterogeneous pnGO nanofluidics. (b) Output current density and (c) power density achieved under three different test conditions as functions of the load resistance.

Transmembrane ion transport and energy conversion behavior

For comparison, we tested the performance of pGO and nGO membranes under the same conditions; short-circuit currents of about 3.1 μA and 13.9 μA were obtained, which are much smaller than that (~35.5 μA) of the heterogeneous pnGO membrane (Fig. 4a). At the nanofluidic interface with fixed surface charges, electrostatic forces repel ions with the same charge as the wall (co-ions) and attract ions with the opposite charge (counter-ions). A region of counter-ions develops in the liquid to maintain the electroneutrality of the solid–liquid interface. The concentrations of local co-ions and counter-ions in the diffusion layer satisfy the Boltzmann distributions:[35,36]

$$n_{co}(x) = n_0 \exp\left(\frac{e\Phi(x)}{k_B T}\right) \quad (1)$$

$$n_{counter}(x) = n_0 \exp\left(-\frac{e\Phi(x)}{k_B T}\right) \quad (2)$$

where n_0 is the bulk solution concentration, e is the elemental charge, $\Phi(x)$ comes from the solution of the classical Poisson–Boltzmann equation (for $x \geq d_{Stern}$ and $\Phi(d_{Stern}) = \xi$), and k_B and T represent Boltzmann's constant and temperature, respectively. The concentration distribution of co-ions and counter-

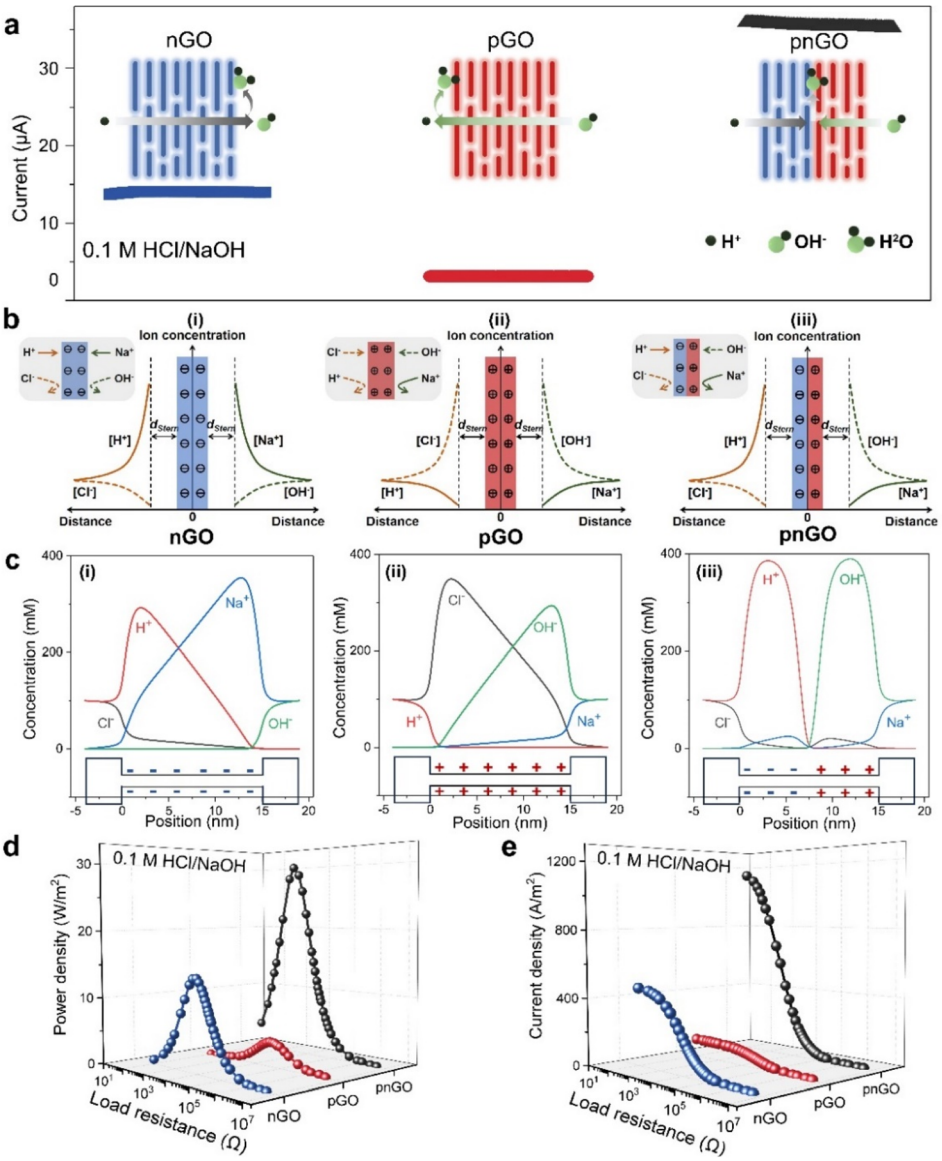

Fig. 4 Transmembrane ion transport and energy conversion behavior. (a) The recorded diffusion current with 0.1 M ABP. (Inset) Schematic illustration of the ion transport in different nanofluidics systems. (b) Co- and counter-ion concentration distributions at the nanofluidic/electrolyte interface. (c) The calculated ion concentration distribution along the centers of the 0.5 nm-sized nanochannels of the three models. The illustrations below correspond to the respective models. (d) Output power density and (e) current density of nGO, pGO, and pnGO membranes with 0.1 M ABP as functions of the load resistance.

ions at the nanofluidic/electrolyte interface is shown in Fig. 4b. For nGO and pGO with a single type of charge, counterions of the same polarity are distributed on both sides of the nanofluidics system (Fig. 4b(i) and (ii)). However, for heterogeneous pnGO nanofluidics (Fig. 4b(iii)), H^+ and OH^- of opposite polarity are distributed on separate sides of the nanofluidics system due to the asymmetric charge distribution. To reveal the origin of the enhanced current output of the pnGO heterogeneous nanofluidics system and explore the mechanism of the ion concentration profile in the confined nanofluidics, finite element method simulations based on the Poisson–Nernst–Planck (PNP) model were performed (see the Experimental section).[40–42] The total length of all simulated models was uniformly set to 15 nm (Fig. S9, ESI†). Three types of 2D nanochannel models are built and the calculated ion concentration distribution along the center of the nanochannel of the three models are shown in Fig. 4c and S10.† The calculated cation and anion concentration profiles at the 2D nanofluidic/electrolyte interface conform to the Boltzmann distribution described above. In Fig. 4c(i), the concentration profile shows that mainly cations (H^+ and Na^+), accumulate in the negatively charged 2D nanochannel driven by a chemical-potential-gradient. In contrast, the ions, mainly anions (OH^- and Cl^-), accumulate strongly when the entire nanochannel is positively charged (Fig. 4c(ii)). By introducing an asymmetric charge distribution, the ion concentration distribution in the 2D

channel changes significantly. Compared to the homogeneous nanofluidics, H^+ and OH^- of opposite polarity are more distributed in the heterogeneous pnGO nanofluidic system, and the concentration profiles are strengthened, consistent with the experimental results (Fig. 4c(iii) and S10†). These results confirm the surface-charge-dependent diffusion-based ion transport behavior and heterogeneous bipolar structure induced ion concentration enhancement.

Under concentration gradients, the total ionic flux N_i depends on the ion diffusion:[40,42]

$$N_i = -D_i \nabla c_i \quad (3)$$

N_i is the ionic flux, D_i is the diffusion coefficient, and c_i is the concentration. D_i is 9.311×10^{-5} cm^2 s^{-1} and 5.273×10^{-5} cm^2 s^{-1} for H^+ and OH^-, respectively. Therefore, under the same concentration gradient, H^+ has a larger flux than OH^-, which determines that the short-circuit current of nGO is higher than that of pGO. Moreover, H^+ in the acid solution and OH^- in the base solution diffuse across the nGO and pGO, respectively, into the heterogeneous interface, and the neutralization reaction "$H^+ + OH^- \rightarrow H_2O$" occurs and the chemical reaction rate v can be calculated by:[18]

$$v = \frac{1}{\nu_B} \frac{dc_B}{dt} \quad (4)$$

where ν_B and c_B refer to the stoichiometric number and concentration of the species, respectively, and t refers to time. Therefore, the higher ion diffusion flux, as well as the "retained" chemical potential gradient caused by the neutralization reaction, are responsible for the considerable current output. As the counter-ions cannot pass through the heterogeneous nanofluidics system, a charge imbalance is established on the two sides of the membrane, inducing a junction potential. The ionic charges can be converted to electronic charges to power an electrical circuit by using two redox electrodes (ESI†). The energy conversion performance was further evaluated by supplying a load resistor (Fig. 4d, e and S11†). As shown in Fig. 4d and e, for pnGO nanofluidics, the current density driven by the chemical potential gradient decreases as the external load increases, and the maximum output power density could reach 29.58 W m^{-2} for 0.1 M ABP, which is superior to that of pGO (3.62 W m^{-2}) and nGO (13.59 W m^{-2}) membranes.

Identifying the role of the heterogeneous structure

We further evaluated the ion diffusion behavior with different ABP concentrations. The short-circuit current (I_{SC}) and open-circuit voltage (V_{OC}) could be obtained from the relevant I–V curves (Fig. S12†).[43] The corresponding obtained I_{SC} and V_{OC} are plotted in Fig. 5a and b. Along with the concentration increases, the I_{SC} and V_{OC} values of all the membranes increase. The V_{OC} of pnGO is comparable to that of pGO, and both are lower than that of nGO (Fig. 5b). However, the I_{SC} of pnGO in Fig. 5a shows a maximum value (22.5 μA) among the three nanofluidics in 0.1 M ABP, which is two times that of nGO (10.2 μA) and six times that of pGO (3.6 μA). This means that the improvement in energy conversion comes from the significant increase in ion flux. As expected, the pnGO with a bipolar charge distribution had the highest power density (Fig. 5c) among the evaluated conditions. To provide new insight into the role of the heterogeneous structure in the ion transport and the power generation process, nGO membranes (nGO_{10} and nGO_{20}) fabricated with 10 mL or 20 mL GO dispersions (1 mg mL^{-1}) were prepared (Fig. 5d). Compared with membranes prepared with the same amount of nanosheets (nGO_{20}), the composite membrane with a heterogeneous structure ($pnGO_{10-10}$) had a lower open circuit voltage due to reduced ion selectivity (Fig. 5f), whereas the transmembrane ion flow was much higher (Fig. 5e). More importantly, the heterogeneous membrane still exhibited an excellent transmembrane ion current, even if the membrane resistance increased due to an extra layer of pGO compared to the nGO_{10} membranes. The enhancement in the energy conversion performance of the composite membrane could be ascribed to the heterogeneous bipolar structure and neutralization reaction. Additionally, the prepared heterogeneous system shows good long-term stability (Fig. S13 and S14†). To provide further physical insight into the synergistic effect of the neutralization reaction and heterogeneous structure, theoretical simulations based on PNP were employed to reveal the energy conversion performance and the distribution of the current density (Fig. 5g and h). With 0.1 M ABP, the current density profile along the center of the channels is plotted from point A to B (Fig. 5h). The current density of model-1 is higher than that of model-2, and model-3 with an asymmetric charge distribution has the highest current density among the three models, which is consistent with our experimental results in Fig. 4e. Additionally, as shown in eqn (3), the ionic flux N_i depends on the ion diffusion. For the nGO side, mainly cations (H^+), accumulate in the negatively charged 2D nanochannel. In contrast, mainly anions (OH^-), accumulate strongly when the nanochannel is positively charged. Therefore, under the same concentration gradient, H^+ has a larger flux than OH^-, which determines that the ion current of the nGO side is higher than that of pGO, showing an asymmetric current density. It has been proven by numerical simulation that the enhanced energy conversion is due to the feasibility of the synergistic effect of the heterogeneous structure and neutralization reaction. To understand the interaction mechanism between specific ions and nanosheets, MD calculations for ion transport in the channels constructed from GO nanosheets were performed (Experimental section, Fig. 5i, j and S15†). According to the simulations, for nGO, H^+ ions could be transported into the nanochannel and interact with $-COO^-$ groups at the edge of the nGO due to electrostatic forces (Fig. 5i). For pGO, OH^- could form hydrogen bonds with the PEI molecule and react with $-NH_3^+$ to form H_2O, which is facilitated by the attraction and bonding between positively and negatively charged molecules (Fig. 5j). MD results indicate the existence of strong interaction forces between nGO/H^+ and pGO/OH^-. We also explored the potential of the system for energy conversion from wastewater using waste acids and bases of unknown composition and concentration from the laboratory (Fig. S16†).

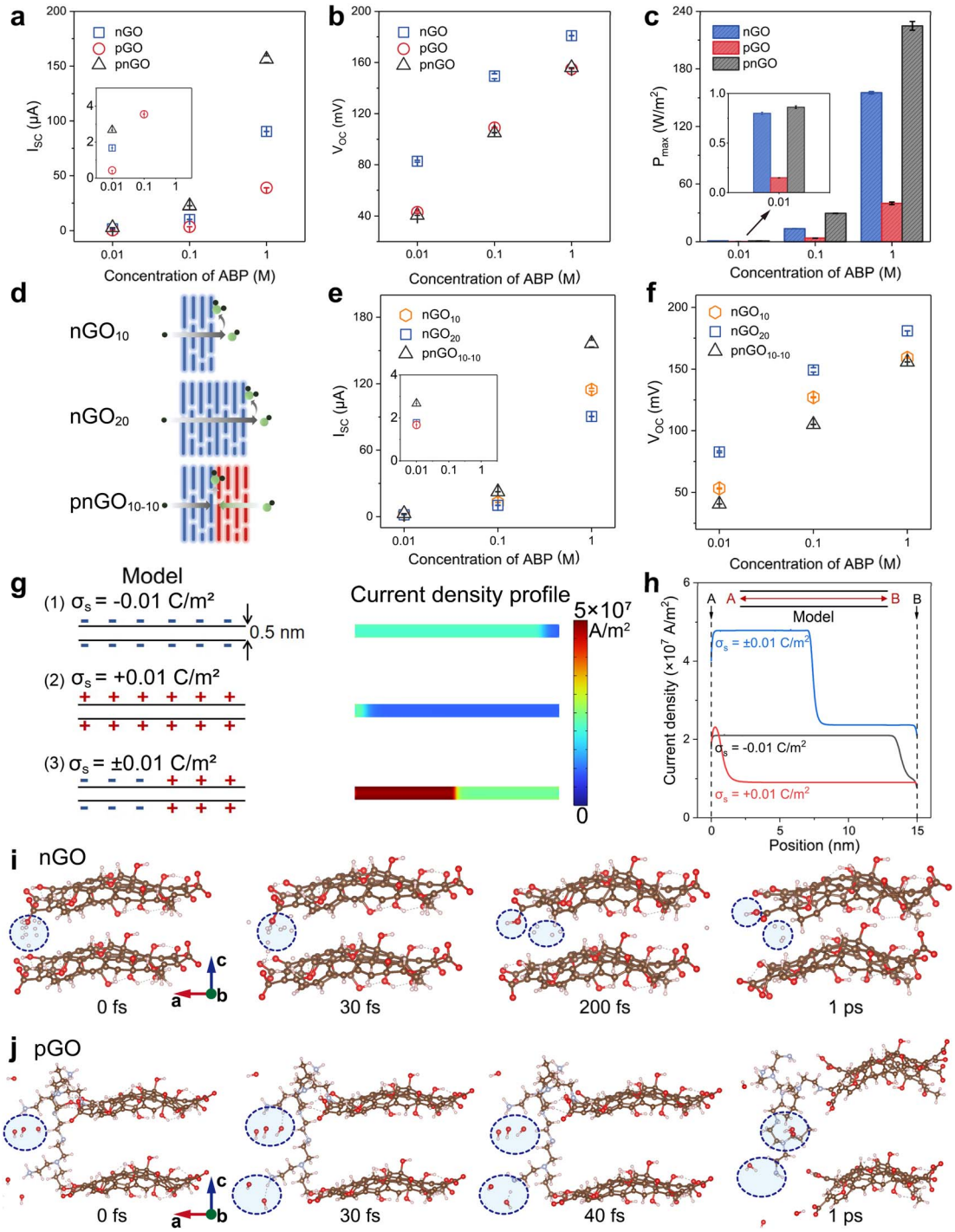

Fig. 5 Identifying the role of the heterogeneous structure. (a and b) Influence of the membrane structure on the I_{SC} and V_{OC} at different ABP concentrations. (c) Comparison of the power density of membranes with homogeneous (pGO and nGO) or heterogeneous (pnGO) structures. (d) Schematic illustration of the ion transport in different nanofluidics systems. (e and f) The I_{SC} and V_{OC} of three different nanofluidics systems at different ABP concentrations. (g) Numerical simulation of the current density profiles based on 2D nanochannels of the three models. (h) The calculated current density distribution along the centers of the 0.5 nm-sized nanochannels of the three models in (g). Representative MD simulation snapshots for two systems: (i) H^+ ion transport within channels constructed from nGO nanosheets. (j) OH^- ion transport within channels constructed from pGO nanosheets.

Conclusions

We report the heterogeneous nanofluidic combination of oppositely charged GO membranes as high-performance power generators to realize the harvesting of ionic power from acid–base neutralization. The pnGO-based energy conversion system exhibited improved ionic transport properties and the highest chemical-potential-driven energy conversion performance as it

benefits from the synergistic effect of the heterogeneous structure and neutralization reaction. More importantly, the synergistic mechanism of the asymmetric charge and neutralization reaction in promoting confined ion transport is innovatively revealed experimentally and theoretically. It is proved that this heterogeneous system provides an ideal platform to harvest the potential energy stored in acid–base neutralization in the form of electrical energy. Moreover, the current research not only provides a new viewpoint of the treatment of industrial acid and alkali waste but also demonstrates the vast potential of the chemical assistance factor in the enhancement of chemical-potential-driven energy conversion. However, waste solutions include lots of impurities in reality. Fouling remains a major challenge for applying membrane technology in real water conditions. In addition to severe biological pollution, organic or inorganic contaminants, in general, can also impair ion transport across the membrane, resulting in a dramatic decrease in ion flux. Another challenge will be to make reliable electrical interfaces with nanofluidic generators because the Ag/AgCl reference electrodes used at present have a limited lifetime. It is clear that the investigation of this system for practical applications is far from complete.

Experimental

Materials and chemicals

The GO dispersion ($\sim$1 mg mL^{-1}) was purchased from XFNANO Materials Tech Co., Ltd, Nanjing, China. 1-(3-Dimethylaminopropyl)-3-ethylcarbo-diimide (EDC, 97%) and polyethyleneimine (PEI-600) were purchased from Beijing InnoChem Science & Technology Co. Ltd. The other chemicals, including hydrochloric acid (HCl), potassium chloride (KCl), and sodium hydroxide (NaOH), were all analytical grade and purchased from Sigma-Aldrich, USA. All aqueous solutions were prepared with degassed Milli-Q water (18.2 MΩ cm). All reagents were directly used without further purification.

Synthesis of pGO

To obtain p-GO, 1-(3-dimethylaminopropyl)-3-ethylcarbo-diimide (EDC, 0.05 g) was added to commercially available GO dispersion (30 mL, $\sim$1 mg mL^{-1}). The mixture was stirred at room temperature for 1 h followed by addition of 0.25 g PEI_{600}. The dispersion was then stirred for an additional 3 h. Then, the precipitate was collected, dispersed in water, and dialyzed for one week to remove residual reactant. Finally, the precipitate was transferred and ultrasonicated to obtain pGO colloidal solution. The colour of the p-GO solution turns brown (0.67 mg mL^{-1}, Fig. S2†).

Material characterizations

The zeta potential of pGO and nGO colloids was measured with a Malvern Zetasizer NanoZS. The microstructures of the membranes were characterized using a scanning electron microscope (Hitachi S-4800, Hitachi, Japan). TEM images were recorded using a transmission electron microscope (JEOL, JEM-2100, Japan). FTIR spectra were recorded using Fourier transform infrared spectroscopy (Excalibur 3100 spectrometer, Varian, USA). The X-ray diffraction tests were conducted using a Bruker D8 Advance powder diffractometer with Cu Kα radiation ($\lambda = 1.5418$ Å) at 40 kV.

Electrical measurement

Electrical measurements of the membranes were carried out using a Keithley 6487 picoammeter (Keithley Instruments, Cleveland, OH). The membranes were fixed between a two-compartment testing cell, adding different salt solutions to carry out transmembrane electrical tests. For the ion transport test, the two compartments were filled with uniform concentration KCl solutions from 1 μM to 1 M. For energy conversion testing, the two halves of the electrochemical cell were populated with acidic solutions and alkaline solutions. At the end of each test, the membrane was rinsed with DI water and drained. The cleaned membrane was rinsed with the solution to be tested before each measurement.

Numerical simulation

The thermoelectric conversion phenomenon was theoretically investigated using commercial finite-element software package COMSOL (version 5.4) Multiphysics based on "electrostatics (Poisson equation)" and "Nernst–Planck without electroneutrality" modules. The coupled governing PNP equations are shown as below:

$$J_i = -D_i\left(\nabla c_i + \frac{z_i F c_i}{RT}\nabla\phi\right) + c_i u \quad (5)$$

$$\nabla^2\varphi = -\frac{F}{\varepsilon}\sum z_i c_i \quad (6)$$

$$\nabla\cdot J_i = 0 \quad (7)$$

Here, the physical quantities J_i, D_i, c_i, z_i, and φ refer to the ionic flux, diffusion coefficient, ion concentration, charge of the species i, and electrical potential, respectively. Eqn (5) is the Nernst–Planck equation, which describes the transport properties of a charged channel. Eqn (6) is the Poisson equation, which describes the relationship between the electrical potential and ion concentrations. The flux should satisfy the time-independent continuity eqn (7) when the system reaches a stationary regime.

The chemical reaction rate constant of acid–base neutralization is determined by the Arrhenius equation, hydrogen ion concentration, and hydroxide ion concentration:

$$K = A\, e^{-\frac{E_a}{RT}} \quad (8)$$

where K represents the chemical rate constant, E_a represents the apparent activation energy, and A represents the pre-exponential factor.

The coupled eqn (5)–(8) must be solved for a given geometry using appropriate boundary conditions.

The boundary condition for the potential φ on the channel wall is:

$$\vec{n}\cdot\nabla\varphi = -\frac{\sigma}{\varepsilon} \quad (9)$$

The ion flux has zero normal components at the boundaries:

$$\vec{n}\cdot J = 0 \quad (10)$$

Then, the ionic current across the reservoirs and nanochannels can be obtained from:

$$I = \int_s F\left(z_p j_p + z_n j_n\right)\cdot\vec{n}\mathrm{d}S \quad (11)$$

The computational domain and model parameters are shown in Fig. S9, ESI.†

Molecular dynamics simulations

Density functional theory (DFT) calculations and MD simulations were performed by using the code Vienna *Ab initio* Simulation Package (VASP),[44] with the Perdew–Burke–Ernzerhof (PBE) functional under the generalized gradient approximation[45] and the projected augmented wave (PAW) pseudopotentials.[46] Ionic relaxations were performed by using the conjugate-gradient algorithm. To correct for the van der Waals interaction, the zero damping DFT-D3 dispersion correction scheme of Grimme was applied.[47] The cutoff energy was set to 400 eV, and the Gaussian smearing width was set to 0.1 eV. In all the calculations, a $1 \times 1 \times 1$ k-point grid centered at the γ point was employed. The MD simulations were carried out with a time step of 1 fs and the Nosé–Hoover thermostat for the NVT canonical ensemble at a temperature of 300 K. The surfaces of both nGO and pGO nanosheets contain various functional groups such as –OH, –COOH, and cyclohexane. The GO surface exhibits curvature due to the structural optimization. In a localized region of the GO edge, a PEI macromolecule replaces one of the $-COO^-$ groups, forming pGO.

Data availability

The data supporting the findings can be found in the article and ESI,† and are available from the authors upon reasonable request.

Author contributions

Pei Liu: conceptualization, methodology, form analysis, investigation, resources, data curation, writing – original draft, writing – review & editing, supervision and project administration. Teng Zhou: software, investigation and resources. Linsen Yang: methodology and resources, writing – review & editing. Xin Li: methodology and investigation. Lei Jiang: conceptualization and supervision. Liping Wen: conceptualization, supervision and project administration.

Conflicts of interest

There are no conflicts to declare.

Acknowledgements

This work was financially supported by the National Natural Science Foundation of China (22305228), the National Key R&D Program of China (2022YFB3805904 and 2022YFB3805900), and the Postdoctoral Fellowship Program of CPSF (Grant Number GZC20232380).

References

1 B. Obama, *Science*, 2017, **355**, 126–129.
2 S.-Y. Pan, Y.-H. Chen, L.-S. Fan, H. Kim, X. Gao, T.-C. Ling, P.-C. Chiang, S.-L. Pei and G. Gu, *Nat. Sustain.*, 2020, **3**, 399–405.
3 S. C. A. Majumdar, *Nature*, 2012, **488**, 294–303.
4 D. J. Davidson, *Nat. Energy*, 2019, **4**, 254–256.
5 Y. Hu, H. Xiao, L. Fu, P. Liu, Y. Wu, W. Chen, Y. Qian, S. Zhou, X. Y. Kong, Z. Zhang, L. Jiang and L. Wen, *Adv. Mater.*, 2023, e2301285.
6 S. Li, J. Wang, Y. Lv, Z. Cui and L. Wang, *Adv. Funct. Mater.*, 2023, **34**, 2308176.
7 L. Ding, M. Zheng, D. Xiao, Z. Zhao, J. Xue, S. Zhang, J. Caro and H. Wang, *Angew. Chem., Int. Ed.*, 2022, **61**, e202206152.
8 A. Siria, M.-L. Bocquet and L. Bocquet, *Nat. Rev. Chem*, 2017, **1**, 0091.
9 Z. Zhang, L. Wen and L. Jiang, *Nat. Rev. Mater.*, 2021, **6**, 622–639.
10 D. Lei, Z. Zhang and L. Jiang, *Chem. Soc. Rev.*, 2024, **53**, 2300–2325.
11 R. Toczyłowska-Mamińska, *Renewable Sustainable Energy Rev.*, 2017, **78**, 764–772.
12 P. Wu, L. Y. Jiang, Z. He and Y. Song, *Environ. Sci.:Water Res. Technol.*, 2017, **3**, 1015–1031.
13 H. Yan, C. Xu, Y. Wu, A. N. Mondal, Y. Wang and T. Xu, *ACS Sustainable Chem. Eng.*, 2017, **5**, 5382–5393.
14 Y. Mei, L. Liu, Y. C. Lu and C. Y. Tang, *Environ. Sci. Technol.*, 2019, **53**, 4640–4647.
15 P. Liu, Y. Sun, C. Zhu, B. Niu, X. Huang, X. Y. Kong, L. Jiang and L. Wen, *Nano Lett.*, 2020, **20**, 3593–3601.
16 W. J. van Egmond, M. Saakes, I. Noor, S. Porada, C. J. N. Buisman and H. V. M. Hamelers, *Int. J. Energy Res.*, 2018, **42**, 1524–1535.
17 Y. Ding, P. Cai and Z. Wen, *Chem. Soc. Rev.*, 2021, **50**, 1495–1511.
18 P. Liu, T. Zhou, L. Yang, C. Zhu, Y. Teng, X.-Y. Kong and L. Wen, *Energy Environ. Sci.*, 2021, **14**, 4400–4409.
19 S. Hong, F. Ming, Y. Shi, R. Li, I. S. Kim, C. Y. Tang, H. N. Alshareef and P. Wang, *ACS Nano*, 2019, **13**, 8917–8925.
20 Z. Zhang, L. He, C. Zhu, Y. Qian, L. Wen and L. Jiang, *Nat. Commun.*, 2020, **11**, 875.
21 Z. Zhang, S. Yang, P. Zhang, J. Zhang, G. Chen and X. Feng, *Nat. Commun.*, 2019, **10**, 2920.
22 X. Zhang, Q. Wen, L. Wang, L. Ding, J. Yang, D. Ji, Y. Zhang, L. Jiang and W. Guo, *ACS Nano*, 2019, **13**, 4238–4245.
23 Q. Wen, P. Jia, L. Cao, J. Li, D. Quan, L. Wang, Y. Zhang, D. Lu, L. Jiang and W. Guo, *Adv. Mater.*, 2020, e1903954.

24 M. Chen, K. Yang, J. Wang, H. Sun, X. H. Xia and C. Wang, *Adv. Funct. Mater.*, 2023, **33**, 2302427.
25 L. Ding, D. Xiao, Z. Lu, J. Deng, Y. Wei, J. Caro and H. Wang, *Angew. Chem., Int. Ed.*, 2020, **59**, 8720–8726.
26 Y. Wu, L. Jiang and L. Wen, *Mater. Today*, 2023, **65**, 189–206.
27 C. Cheng, G. Jiang, C. J. Garvey, Y. Wang, G. P. Simon, J. Z. Liu and D. Li, *Sci. Adv.*, 2016, **2**, e1501272.
28 D. Quan, D. Ji, Q. Wen, L. Du, L. Wang, P. Jia, D. Liu, L. Ding, H. Dong, D. Lu, L. Jiang and W. Guo, *Adv. Funct. Mater.*, 2020, 2001549.
29 J. Ji, Q. Kang, Y. Zhou, Y. Feng, X. Chen, J. Yuan, W. Guo, Y. Wei and L. Jiang, *Adv. Funct. Mater.*, 2016, **27**, 1603623.
30 W. Tian, A. VahidMohammadi, Z. Wang, L. Ouyang, M. Beidaghi and M. M. Hamedi, *Nat. Commun.*, 2019, **10**, 2558.
31 L. Chen, G. Shi, J. Shen, B. Peng, B. Zhang, Y. Wang, F. Bian, J. Wang, D. Li, Z. Qian, G. Xu, G. Liu, J. Zeng, L. Zhang, Y. Yang, G. Zhou, M. Wu, W. Jin, J. Li and H. Fang, *Nature*, 2017, **550**, 380–383.
32 M. J. Allen, V. C. Tung and R. B. Kaner, *Chem. Rev.*, 2010, **110**, 132.
33 J. Hao, R. Wu, J. Zhou, Y. Zhou and L. Jiang, *Nano Today*, 2022, **46**, 101593.
34 R. Fan, S. Huh, R. Yan, J. Arnold and P. Yang, *Nat. Mater.*, 2008, **7**, 303–307.
35 R. B. Schoch, J. Han and P. Renaud, *Rev. Mod. Phys.*, 2008, **80**, 839–883.
36 M. A. Brown, A. Goel and Z. Abbas, *Angew. Chem., Int. Ed.*, 2016, **55**, 3790–3794.
37 J. Feng, M. Graf, K. Liu, D. Ovchinnikov, D. Dumcenco, M. Heiranian, V. Nandigana, N. R. Aluru, A. Kis and A. Radenovic, *Nature*, 2016, **536**, 197–200.
38 R. E. Pattle, *Nature*, 1954, **174**, 660.
39 D.-K. Kim, C. Duan, Y.-F. Chen and A. Majumdar, *Microfluid. Nanofluid.*, 2010, **9**, 1215–1224.
40 H. S. White and A. Bund, *Langmuir*, 2008, **24**, 2212–2218.
41 C. G. Gray and P. J. Stiles, *Eur. J. Phys.*, 2018, **39**, 053002.
42 D. Constantin and Z. S. Siwy, *Phys. Rev. E*, 2007, **76**, 041202.
43 X. Liu, M. He, D. Calvani, H. Qi, K. Gupta, H. J. M. de Groot, G. J. A. Sevink, F. Buda, U. Kaiser and G. F. Schneider, *Nat. Nanotechnol.*, 2020, **15**, 307–312.
44 G. Kresse and J. Furthmüller, *Phys. Rev. B:Condens. Matter Mater. Phys.*, 1996, **54**, 11169–11186.
45 J. P. Perdew, K. Burke and M. Ernzerhof, *Phys. Rev. Lett.*, 1996, **77**, 1396.
46 P. E. Blöchl, *Phys. Rev. B:Condens. Matter Mater. Phys.*, 1994, **50**, 17953–17979.
47 S. Grimme, J. Antony, S. Ehrlich and H. Krieg, *J. Chem. Phys.*, 2010, **132**, 154104.